

Corona-heated Accretion-disk Reprocessing: Frequency-Resolved Lag Predictions for UV/Optical Reverberation Mapping of Active Galactic Nuclei

JIE CHEN ^{1,2,3} MOUYUAN SUN ¹ AND ZHI-XIANG ZHANG ¹

¹*Department of Astronomy, Xiamen University, Xiamen, Fujian 361005, China; msun88@xmu.edu.cn*

²*Department of Astronomy, School of Physics, Peking University, Beijing 100871, China*

³*Kavli Institute for Astronomy and Astrophysics, Peking University, Beijing 100871, China*

ABSTRACT

Continuum reverberation mapping with high-cadence, long-term UV/optical monitoring of Active Galactic Nuclei (AGNs) enables us to resolve the AGN central engine sizes on different timescales. The frequency-resolved time lags of NGC 5548 (the target for the AGN STORM I campaign) are inconsistent with the X-ray reprocessing of the classical Shakura & Sunyaev disk model. Here we show that the frequency-resolved time lags in NGC 5548 can be well produced by the Corona-Heated Accretion-disk Reprocessing (CHAR) model. Moreover, we make the CHAR model predictions of the frequency-resolved time lags for Mrk 817, the source of the AGN STORM II campaign. We also obtain the frequency-resolved time lags as a function of the black-hole mass and Eddington ratio, which is valid for black-hole masses from $10^{6.5}$ to $10^9 M_{\odot}$, and Eddington ratios from 0.01 to 1. Moreover, we demonstrate that, with the time spans of current continuum reverberation-mapping campaigns, the lag-luminosity relation of the CHAR model can be $\tau_{\text{gz}} \propto L_{5100}^{0.55 \pm 0.04}$, which is consistent with observations. Future observations can test our results and shed new light on resolving the AGN central engine.

Keywords: Accretion (14); Active galactic nuclei (16); Supermassive black holes (1663)

1. INTRODUCTION

Active Galactic Nuclei (AGNs) show strong electromagnetic radiations across the entire spectrum and are powered by the accretion of a central supermassive black hole (SMBH). One popular model to describe the SMBH gas accretion in AGNs is the geometrically thin but optically thick disk (i.e., the standard thin-disk model; Shakura & Sunyaev 1973). In most cases, the SMBH accretion disks are too small to be resolved spatially with current facilities. There have been many efforts to achieve high spatial resolution in the time domain. Reverberation Mapping (RM; Blandford & McKee 1982) is a method to obtain the emission-region sizes by measuring the time lags between light curves of different wavelengths. The RM method is first widely used to measure broad-line region (BLR) sizes and estimate black-hole masses and is now widespread in determining accretion-disk sizes (for a review, see Cackett et al. 2021). For the

accretion-disk RM, the underlying assumption is that the flux variations at various wavelengths are driven by the reprocessing of the same variable X-ray irradiation from the corona (hereafter, the X-ray reprocessing). Hence, the observed time lag between the X-ray emission and the reprocessed one is simply the light travel time for the X-ray to reach the accretion disk. To be precise, the radiation at a given wavelength of the accretion disk is produced by numerous parts of the disk with different temperatures, and the measured time lag is, therefore, an averaged value over the entire accretion disk weighted by variability amplitudes.

Recent intensive UV/optical continuum reverberation mappings find that some AGNs' continuum time lags are typically 2–3 times larger than the prediction from the standard thin-disk model with X-ray reprocessing (e.g., Edelson et al. 2015; Fausnaugh et al. 2016; Cackett et al. 2018; Fausnaugh et al. 2018; Kara et al. 2021; Donnan et al. 2023; Kara et al. 2023). Several models have been proposed to account for the discrepancy. Often, these models argue that the X-ray reprocessing of the standard thin disk should be revised to include the reprocessing of BLR clouds (Cackett et al. 2018;

Chelouche et al. 2019; Korista & Goad 2019) or disk winds (Sun et al. 2019). According to the popular BLR model, the diffuse continua from the BLR clouds make a substantial or even dominant contribution to the optical variability and also continuum reverberation lags (e.g., Cackett et al. 2018; Lawther et al. 2018; Sun et al. 2018b; Chelouche et al. 2019; Korista & Goad 2019; Guo et al. 2022; Netzer 2022). If this is indeed the case, the observed luminosity of an AGN then does not fully characterize its accretion rate. Other works suspect that the X-ray corona has a large and highly variable scale height (Kammoun et al. 2019, 2021a,b, 2023). Some models replace the X-ray reprocessing with alternative mechanisms. For instance, Gardner & Done (2017) suggest that an ‘‘FUV torus’’ is formed in the inner disk and can heat the outer disk. Sun et al. (2020) propose the Corona Heated Accretion-disk Reprocessing (CHAR) model, in which the corona and disk are coupled via magnetic fields. Hence, the magnetic turbulence in the corona can change the disk heating rate and induce disk temperature fluctuations. The CHAR model can explain the larger-than-expected accretion disk sizes without X-ray reprocessing or the diffuse continuum emission from BLR (see Sun et al. 2020). The anti-correlation between the ratio of the observed time lag to the standard thin-disk prediction and the luminosity favors the BLR or the CHAR model (Li et al. 2021). Generally, the physics of the variability process in UV/optical is still an unsettled issue.

Popular methods for measuring RM time lags are the cross-correlation function (CCF; Peterson et al. 1998) and the Fourier analysis (for a review, see Uttley et al. 2014). The cross-correlation function measures the correlation between the light curves of two wavelengths at each lag. The Fourier analysis calculates the phase lag of the cross-power spectrum at each frequency (see Section 2 and Uttley et al. 2014). The Fourier analysis can therefore separate lags from different processes occurring on different timescales. The Fourier analysis is widely used in X-ray RMs because of the rapid variability and high cadence in X-ray light curves. The optical light curves, however, often have a low cadence and short time duration compared with the timescale of interest, making Fourier analysis challenging to apply.

Benefiting from the high-cadence observations with *Swift* (Roming et al. 2005) and ground-based telescopes, and also the techniques dealing with gaps in light curves (e.g., the maximum likelihood approach; Miller et al. 2010; Zoghbi et al. 2013; Cackett et al. 2022), the Fourier analysis has been applied in analyzing the AGN Space Telescope and Optical Reverberation Mapping (AGN STORM I; De Rosa et al. 2015) data of NGC

5548 (Cackett et al. 2022). The authors find that the UV/optical lags in NGC 5548 generally decrease with increasing frequency. This trend can not easily be described by the X-ray reprocessing of a large accretion disk alone. Instead, a standard thin disk with the diffuse continuum emission from the BLR can explain the observations. Alternatively, the CHAR model has predicted a similar trend of the frequency-resolved time lags (see fig. 7 of Sun et al. 2020). Recently, the frequency-resolved UV/optical time lags of a second source, Mrk 335, were presented by Lewin et al. (2023). Hence, we are motivated to quantitatively compare the CHAR model with the frequency-resolved time lags of NGC 5548 and Mrk 335. Mrk 817 is the target for the AGN STORM II program (Kara et al. 2021). We, therefore, aim to predict its frequency-resolved time lags, which can be tested by future AGN STORM II data. We also provide analytical functions to describe the CHAR frequency-resolved lags as a function of black-hole mass and Eddington ratio for future observational testings.

This manuscript is formatted as follows. In Section 2, we introduce the frequency-resolved time lags. In Section 3, we present the frequency-resolved time-lag predictions of the CHAR model for three AGNs, NGC 5548, Mrk 335, and Mrk 817. In Section 4, we show the frequency-resolved lags as a function of black-hole mass and Eddington ratio. In Section 5, we discuss the lag-luminosity relation of the CHAR model. Summary is made in Section 6. Note that the Schwarzschild radius $R_s \equiv 2GM_{\text{BH}}/c^2$, where G and c are the gravitational constant and speed of light, respectively. The Eddington luminosity is $L_{\text{Edd}} = 1.3 \times 10^{38} (M_{\text{BH}}/M_{\odot}) \text{ erg s}^{-1}$.

2. FREQUENCY-RESOLVED LAGS

Time series can be analyzed in the time and frequency domain. In reverberation mapping studies, a widely known time-domain technique used in measuring time lags between two light curves is the cross-correlation function (CCF; Peterson et al. 1998). The frequency analysis technique, on the other hand, acts as a filter on light curves and estimates the time lag at each Fourier frequency or timescale (see sections 2.1.2 and 2.4.3 of Uttley et al. 2014). Here, we briefly explain the mathematics of the frequency-resolved lags.

For light curves of two wavebands $x(t)$ and $y(t)$, their n th value of discrete Fourier transforms are as a function of the Fourier frequency $f_n = n/(N\Delta t)$, where N and Δt are the numbers of data points and cadence of the light curve, respectively; i.e.,

$$X_n = \sum_{k=0}^{N-1} x_k \exp(-2\pi ink/N) = A_{x,n} \exp(i\varphi_{x,n}), \quad (1)$$

$$Y_n = \sum_{k=0}^{N-1} y_k \exp(-2\pi ink/N) = A_{y,n} \exp(i\varphi_{y,n}), \quad (2)$$

where x_k and y_k are the k th values of the light curves. These discrete Fourier transforms can be expressed as an amplitude ($A_{x,n}$ or $A_{y,n}$) and a phase ($\varphi_{x,n}$ or $\varphi_{y,n}$). If $y(t)$ has an additional phase-shift ϕ_n with respect to $x(t)$ at frequency f_n , we expect that

$$Y_n = A_{y,n} \exp[i(\varphi_{x,n} + \phi_n)], \quad (3)$$

and their cross-power spectrum

$$C_{xy,n} = X_n^* Y_n = A_{x,n} A_{y,n} \exp(i\phi_n). \quad (4)$$

Then, the time lag at frequency f_n is

$$T_{\text{lag}}(f_n) = \phi_n / (2\pi f_n). \quad (5)$$

Using this technique, we can obtain the lags at each frequency ranging from $f_{\text{min}} = 1/T_{\text{obs}} = 1/(N\Delta t)$ to the Nyquist frequency $f_{\text{max}} = 1/(2\Delta t)$.

Compared to CCF, the Fourier analysis provides a more straightforward way for revealing the reverberation mapping features hidden in the data. In X-ray RMs, for example, the positive time lags between soft and hard X-rays on short timescales are considered to be the light travel time between the direct power-law X-ray emission of the corona and the reflected component of the disk (for a review, see Uttley et al. 2014). On the other hand, the negative time lags on long timescales indicate disk variability propagates from the disk to the corona. Strictly speaking, both the corona and disk produce soft X-ray emission, so the measured time lags on short timescales can be less than the true light travel time from the corona to the disk, and the shape of the lag-frequency relationship will be changed to some extent (i.e., the dilution effect; see section 4.1.1 and fig. 20 of Uttley et al. 2014). Since the size of the accretion disk is much larger than the X-ray corona, the dilution effect in UV/optical RMs is more severe than in X-ray. Therefore, the frequency-resolved time lags of two disk continuum light curves are more complicated than in X-ray studies, which depend upon the overlapping in their emission regions and also possibly on the variability timescale (see Appendixes A & B). In summary, the frequency-resolved time lags can tell us the details of the physical process for variability and emission.

To our best knowledge, the Fourier technique has been used to measure the frequency-resolved time lags of the AGN STORM I target NGC 5548 (Cackett et al. 2022), and other sources, e.g., Mrk 335 (Lewin et al. 2023) and Fairall 9 (but with large uncertainties; Yao et al. 2023). The frequency-resolved time lags of NGC 5548

from Cackett et al. (2022) show that the X-ray reprocessing of a large accretion disk produces excessive lags in high frequency and less lags in low frequency. Hence, it leads to attempts to use the BLR model (see fig. 4 in Cackett et al. 2022) or the CHAR model to account for the frequency-resolved lags. Since NGC 5548 has the most bands and highest cadences (i.e., the best-studied reverberation mapping AGN), we here choose it to test the CHAR model. We also examine the recent results of Mrk 335.

3. FREQUENCY-RESOLVED LAGS OF THE CHAR MODEL IN THE AGN STORM TARGETS

3.1. NGC 5548

We calculate the frequency-resolved lags for light curves on NGC 5548 from the CHAR model of Sun et al. (2020) and compare them with the results from Cackett et al. (2022). Here we briefly introduce the CHAR model. The CHAR model is based on the physical picture that, the chaotic magnetohydrodynamic (MHD) fluctuations in the corona propagate into the accretion disk and alter the disk MHD turbulence dissipation rate, which is also the accretion-disk gas heating rate. Then, the disk temperature fluctuates in response to the variable heating rate. The CHAR model assumes the disk keeps vertical hydrostatic equilibrium. Given the PSD of the heating-rate fluctuations and initial temperature conditions of a standard thin disk, the temperature fluctuations can be determined by solving the equation for vertical integrated thermal-energy conservation (for a detailed description, see section 2 of Sun et al. 2020). Hence, the CHAR model has three parameters introduced by the standard thin disk, namely, the black-hole mass (M_{BH}), Eddington ratio¹ ($L_{\text{bol}}/L_{\text{Edd}}$, where L_{bol} is bolometric luminosity), and the dimensionless viscosity parameter (α). Given these three parameters, the CHAR model can generate simulated light curves for the fixed wavelengths by integrating the multi-temperature blackbody emission over the whole accretion disk. We stress that general relativistic effects and color corrections are not considered in the calculation; hence, the results are valid for those bands whose corresponding emission regions are not close to the SMBH event horizon. Otherwise, the calculated time lags underestimate the true time lag (the demonstration of the general relativistic effects for the X-ray reprocessing is

¹ One of the parameters of the CHAR model is the dimensionless accretion rate \dot{m} . Here, $\dot{m} = \dot{M}/\dot{M}_{\text{Edd}}$, where the absolute accretion rate $\dot{M} = L_{\text{bol}}/(\eta c^2)$, and the Eddington accretion rate $\dot{M}_{\text{Edd}} = 10L_{\text{Edd}}/c^2$. η is the radiative efficiency. We use $\eta = 0.1$ to estimate M . Hence, \dot{m} also represents the Eddington ratio.

given by, e.g., Kammoun et al. 2023), and this underestimation on longer timescales is weaker than on short timescales. Following previous studies of NGC 5548, we fix $M_{\text{BH}} = 5 \times 10^7 M_{\odot}$ (Edelson et al. 2015; Fausnaugh et al. 2016) and $L_{\text{bol}}/L_{\text{Edd}} = 0.02$ (here, we, for simplicity, assume the disk is face-on). The remaining parameter $\alpha = 0.2$ (e.g., King et al. 2007). The inner and outer boundaries of the accretion disk are fixed to be $3 R_s$ and $30,000 R_s$, respectively. Hence, there are no free parameters in our calculation. In our simulations, we adopt the redshift $z = 0.017175$ (De Rosa et al. 2015) and generate the simulated light curves of all 18 UV/optical bands listed in Table 5 of Fausnaugh et al. (2016). Each light curve spans 170 days with a cadence of 0.1 days. Our simulation is repeated 512 times to account for the statistical fluctuations due to the limited time duration.

We adopt the Fourier technique outlined in Section 2 to measure frequency-resolved time lags in the NGC 5548 simulated light curves. All the lags are measured with respect to the 1158 Å emission (i.e., the same as Cackett et al. 2022) by the standard fast Fourier technique. The median lags of the 512 CHAR results are shown as the purple curves in Fig. 1. We use the 16-th and 84-th percentiles of the 512 simulations as 1σ uncertainties (i.e., the dark purple shaded areas), and the 2.5-th and 97.5-th percentiles as the 2σ uncertainties (i.e., the light purple shaded areas).

Our simulated lag-frequency relation agrees well with the observations of NGC 5548 (Cackett et al. 2022) for all bands in Fig. 1. Like real observations, the simulated lags decrease with increasing frequency. Quantitatively, we use the reduced chi-square χ_{reduced}^2 to measure the goodness of fit between the model and observations, which is defined as the ratio of χ^2 to the degrees of freedom (DOF). Here the statistic χ^2 is defined as

$$\chi^2 = \sum_{i=1}^N \frac{(y_{i,\text{model}} - y_{i,\text{data}})^2}{\sigma_{i,\text{model}}^2 + \sigma_{i,\text{data}}^2}, \quad (6)$$

where y_i and σ_i are the time lag value and its 1σ uncertainty from real data and the model, respectively. For the CHAR model, $\chi^2 = 95.01$ for 81 data points without free parameters, giving $\chi_{\text{reduced}}^2 = 1.173$. In the modeling of the small disk plus BLR model (Cackett et al. 2022), $\chi^2 = 70.95$ for 81 data points and 17 free parameters, giving $\chi_{\text{reduced}}^2 = 1.109$; for the X-ray reprocessing of a large accretion disk model, $\chi^2 = 236.4$ for 81 data points without free parameters, giving $\chi_{\text{reduced}}^2 = 2.919$ (Cackett et al. 2022). Hence, the CHAR model performs similarly to the small disk plus BLR model, and both models are better than the X-ray reprocessing model.

In the CHAR model, the time lag between light curves of two wavelengths comes from two physical processes,

i.e., the propagation of coronal magnetic fluctuations and the disk heating process by magnetic fluctuations. The former is near to the light travel time, and the latter is thermal timescale ($\tau_{\text{TH}} \sim 1/(\alpha\Omega_{\text{K}})$, where Ω_{K} is Keplerian angular velocity; this is the gas temperature fluctuation timescale in the CHAR model). The thermal timescale indicates a slower temperature response for gas in the outer regions than in the inner parts, contributing large time lags on long timescales (Sun et al. 2020). Unlike the BLR model whose response function is a summation of the disk and BLR components with variable fraction, the CHAR model considers the magnetohydrodynamic of the accretion disk itself, which can explain the frequency-resolved lags of NGC 5548.

We also consider the case of $\alpha = 0.01$ and find that the time lags of the model are smaller than lags from the observations, which suggests that $\alpha \simeq 0.2$ may be more consistent with real cases (King et al. 2007).

3.2. Mrk 335

Very recently, the frequency-resolved lags in Mrk 335 were obtained by Lewin et al. (2023). Here we run 512 CHAR model simulations for Mrk 335 with $M_{\text{BH}} = 1.69 \times 10^7 M_{\odot}$ (Grier et al. 2012), $L/L_{\text{Edd}} = 0.07$ (Tripathi et al. 2020), and redshift $z = 0.025785$ (Huchra et al. 1999). For the simulated light curves, the time duration in each band is 100 days with a cadence of 0.3 days. We present the UV/optical lag-frequency relations with respect to the UVW2 band in Fig. 2. The CHAR model agrees well with the observations. Quantitatively, $\chi^2 = 49.79$ for 45 data points without free parameters, gives $\chi_{\text{reduced}}^2 = 1.107$.

3.3. Mrk 817

The target for the AGN STORM II campaign is the Seyfert 1 galaxy Mrk 817, whose mass is similar to that of NGC 5548 but more luminous. Two essential CHAR model parameters of Mrk 817 are from Kara et al. (2021): the black-hole mass $M_{\text{BH}} = 3.85 \times 10^7 M_{\odot}$, and the Eddington ratio $L/L_{\text{Edd}} = 0.2$. We run a similar simulation with the redshift $z = 0.031455$ for Mrk 817 (Strauss & Huchra 1988). For the simulated light curves, the time duration in each band is 200 days with a cadence of 0.1 days. We present the lag-frequency predictions for Mrk 817 in Fig. 3, and these simulated results can be tested by the Mrk 817 AGN-STORM II observations.

4. TRENDS OF FREQUENCY-RESOLVED LAGS IN THE CHAR MODEL

In the CHAR model, the rest-frame time lag (T_{lag}) is a function of the variability frequency (f), wavelength

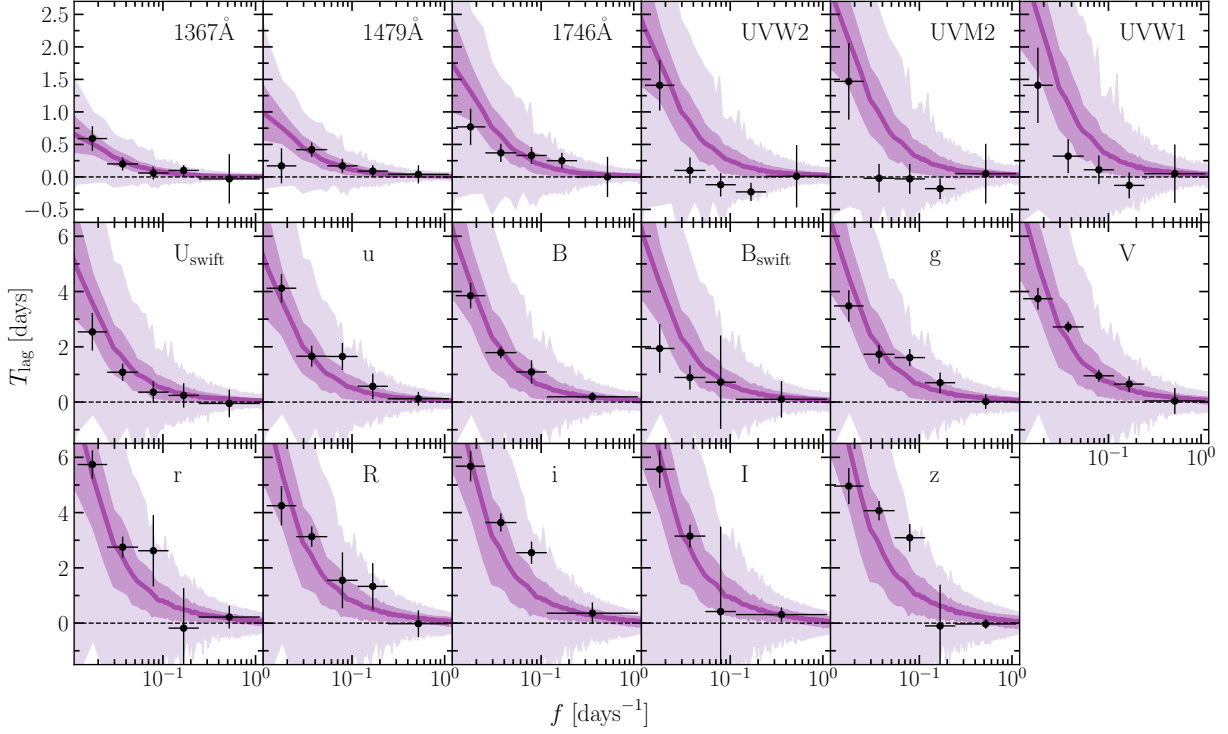


Figure 1. Simulated frequency-resolved lags in NGC 5548. The frequency range is $0.011\text{--}1.21\text{ days}^{-1}$. The purple curves represent the median lags in the 512 CHAR simulations; the dark purple shaded areas correspond to the 16-th and 84-th percentiles (i.e., the 1σ uncertainties), and light purple shaded areas correspond to the 2.5-th and 97.5-th percentiles (i.e., the 2σ uncertainties). Black dots with error bars are the frequency-resolved lags and their 1σ uncertainties from [Cackett et al. \(2022\)](#), who measured the time lags from the NGC 5548 AGN STORM I observations. Note that the y-axis ranges in the top panels are narrower than those of the middle and bottom panels. The simulated frequency-resolved lags for NGC 5548 from the CHAR model without free parameters are broadly consistent with observations.

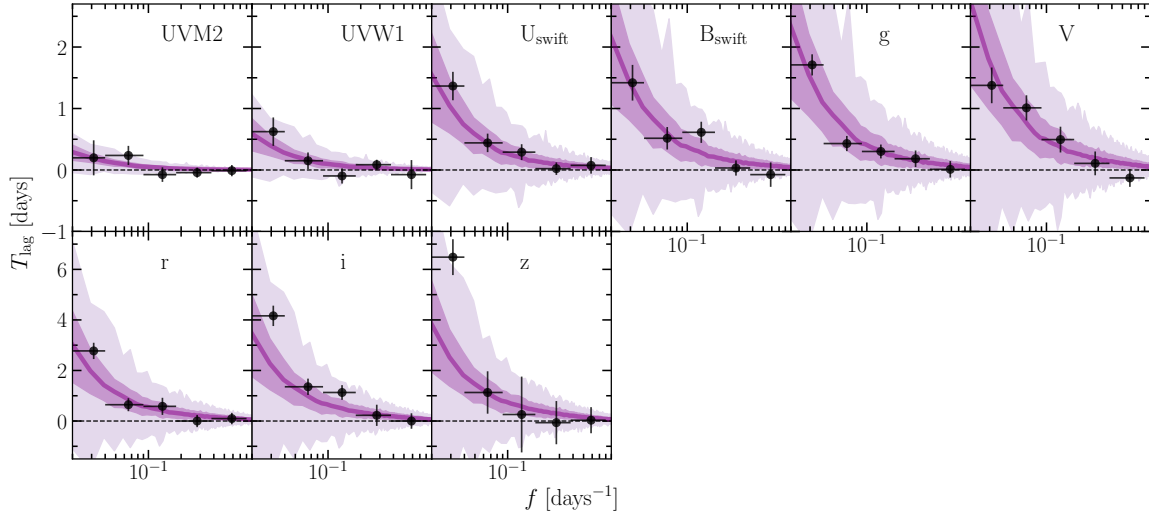


Figure 2. Simulated frequency-resolved lags in Mrk 335 with respect to the UVW2 band. The frequency range is $0.02\text{--}0.9\text{ days}^{-1}$. Black dots with error bars are the frequency-resolved lags and their 1σ uncertainties from [Lewin et al. \(2023\)](#). The simulated frequency-resolved lags for Mrk 335 from the CHAR model are broadly consistent with observations.

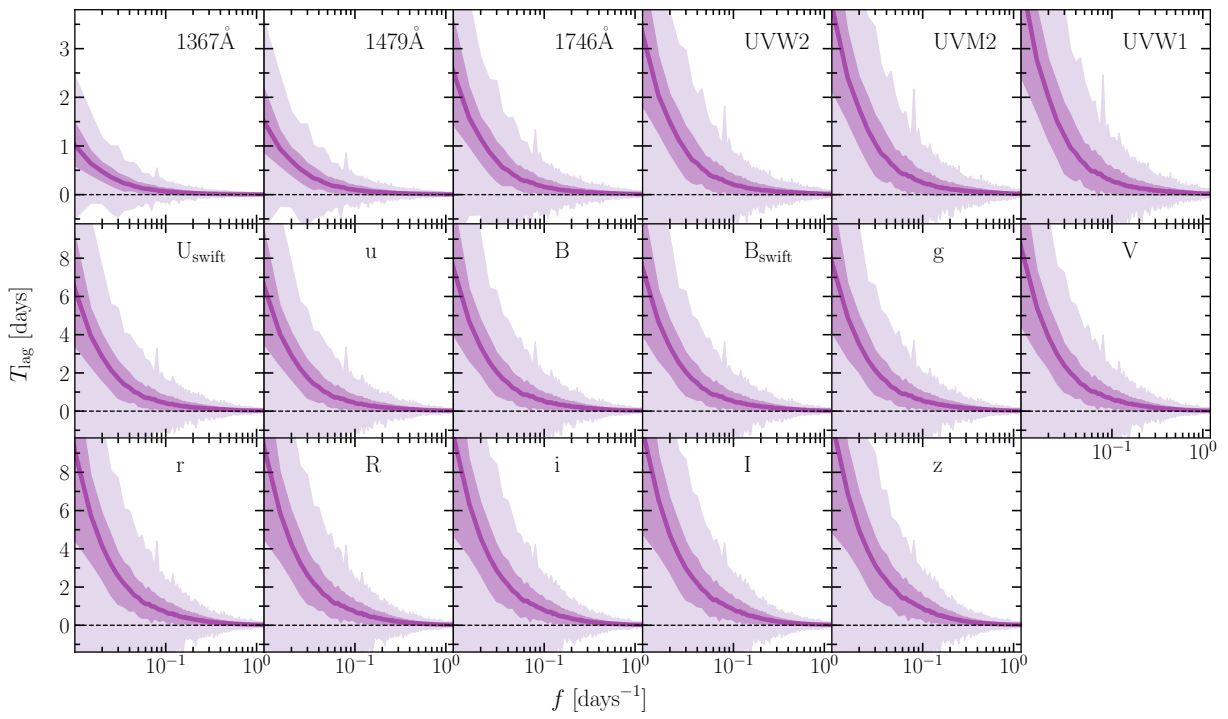


Figure 3. Similar to Fig. 1, but for Mrk 817.

(λ), black-hole mass (M_{BH}), and Eddington ratio (\dot{m}) in terms of $T_{\text{lag}} = g(f, \lambda, M_{\text{BH}}, \dot{m})$. For giving a comprehensive prediction, we simulate 30 cases in the parameter space of M_{BH} and \dot{m} ; then, we calculate the corresponding frequency-resolved lags. These 30 cases are selected as follows: M_{BH} ranges from $10^{6.5}$ to $10^9 M_{\odot}$, with six values in equal logarithmic increments; \dot{m} ranges from 0.01 to 1, with five values in equal logarithmic increments. We generate the simulated light curves of 18 UV/optical bands like NGC 5548. The time duration in each band is 400 days with a cadence of 0.1 days. Each case is repeated 512 times in CHAR simulations. Based on the CHAR simulated light curves of the 30 mock sources, we compute the frequency-resolved lags with respect to the 1158 Å emission. The lag-frequency relations are available in the FITS file format and can be accessed from <https://doi.org/10.12149/101308>.

We explore the dependence of lags upon M_{BH} , \dot{m} , and f by considering the lags between the V band (5404 Å) and 1158 Å emission. We show the frequency-resolved lags for the 30 mock cases in Figs. 4 and 5. Each panel in Fig. 4 shows the frequency-lag relation at a fixed mass for different Eddington ratios; each panel in Fig. 5 illustrates the frequency-lag relation at a fixed Eddington ratio for different black-hole masses. For clarity, the error bars are not shown.

On long timescales or low frequency (e.g., $\sim 0.01 \text{ days}^{-1}$), the relation between the time lags and Eddington ratio or luminosity, as the M_{BH} increases, changes from positive to nearly negative. We discuss this interesting phenomenon, and the possible reasons are as follows. Qualitatively, as black-hole mass or Eddington ratio increases, the emission regions of a given wavelength increase due to the larger accretion disk or higher effective temperature, respectively. To quantify the dominant position of the emission regions for a given wavelength, we calculate the half-light radius (R_{half}) of the time-variable emission following Tie & Kochanek (2018). First, we obtain the first-order Taylor expansion of the Planck function at each radius (i.e., $\Delta B(\lambda, R)$; eq. 19 from Sun et al. 2020), which represents the variation of intensity as a function of radius. We then calculate the cumulative contribution fraction of $\leq R$ regions to the total variability by

$$f_{\Delta L}(\lambda, R) = \frac{\int_{R_{\text{in}}}^R \Delta B(\lambda, r) r dr}{\int_{R_{\text{in}}}^{R_{\text{out}}} \Delta B(\lambda, r) r dr}, \quad (7)$$

where R_{in} and R_{out} are the inner and outer boundaries of the accretion disk, respectively. The half-light radius of the variable flux is calculated by setting $f_{\Delta L}(\lambda, R_{\text{half}}) = 0.5$. We obtain $\Delta R_{\text{half}} = R_{\text{half}, 5404} - R_{\text{half}, 1158}$ in a range of black-hole masses with $\dot{m} = 0.1$

in Fig. 6. Consistent with our expectations, the relative distance between the emission regions of the two wavelengths increases with black-hole mass.

The time lag, however, does not necessarily increase with the relative distance. The first reason is the dilution effect, which is caused by the fact the emission regions of the shorter wavelength can significantly overlap with those of the longer wavelength (Uttley et al. 2014). Hence, the measured lag of the two bands depends upon not only the relative distance but also the overlapping of their emission regions. The larger overlapping gives a shorter lag; an example is presented in Appendix A. Here we define the overlapping degree as

$$p_{\text{ov}} = 1 - \frac{R_{\text{half}, 5404} - R_{\text{half}, 1158}}{R_{\text{half}, 5404} + R_{\text{half}, 1158}}. \quad (8)$$

We can obtain the overlapping degrees on different timescales. The relationship between overlapping and M_{BH} is shown in Fig. 7. It shows that the shorter timescale and larger M_{BH} result in a higher degree of overlapping and, therefore, smaller lags in high-luminosity sources. The frequency-resolve time lags also depend upon the variability timescale. We find that the larger variability timescale also gives shorter measured lags (for a detailed discussion, see Appendix B). Since the thermal timescale at a fixed radius increases with mass or luminosity, the times lags in high-luminosity sources will decrease accordingly. In summary, these two effects can explain the smaller lags in large black-hole mass or high-luminosity sources.

To find the mathematical form of $T_{\text{lag}} = g(f, \lambda, M_{\text{BH}}, \dot{m})$ from our CHAR simulations, we assume the function takes the following form for each M_{BH} and \dot{m} ,

$$T_{\text{lag}} = \left(\frac{\lambda}{\lambda_0} - 1\right)^\beta \frac{T_0}{f + f_0}, \quad (9)$$

where $\lambda_0 = 1158 \text{ Å}$. The coefficients β , f_0 , and T_0 depend upon M_{BH} and \dot{m} . In our fitting, T_{lag} , f , and M_{BH} are in units of days, days^{-1} , and M_{\odot} , respectively. The frequency range in our fitting is $0.0073\text{--}4.47 \text{ days}^{-1}$. At very high frequencies (e.g., $f > 2 \text{ days}^{-1}$ for $M_{\text{BH}} = 10^{6.5} M_{\odot}$; $f > 1 \text{ days}^{-1}$ for $M_{\text{BH}} = 10^7 M_{\odot}$), the correlation between T_{lag} and λ is weak. To reject these frequencies from the fitting, we calculate the Pearson correlation coefficient (r) between T_{lag} and $\log(\lambda/\lambda_0 - 1)$ for each frequency, M_{BH} , and \dot{m} . For each combination of M_{BH} and \dot{m} , we select frequency-resolved lags with r^2 greater than 0.9 and then fit them with Eq. 9. We obtain the best-fitting β , f_0 , and T_0 for each M_{BH} and \dot{m} combination. We then use the second-order polynomials to fit the relations among these coefficients,

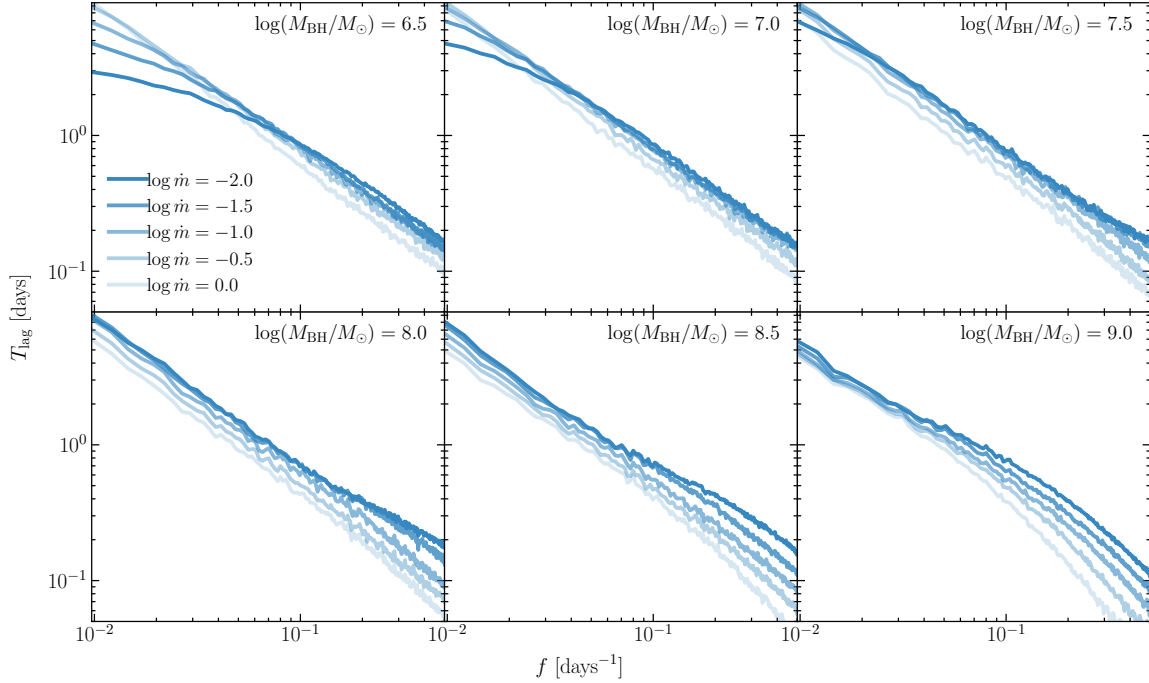


Figure 4. Simulated frequency-resolved lags of 5404 Å (i.e., *V* band) vs 1158 Å for the 30 cases. The frequency range is 0.097–0.5 days^{−1}. Each panel represents the frequency-lag relation at a fixed black-hole mass for different Eddington ratios. The lighter blue color corresponds to a larger accretion rate. On the low-frequency region (e.g., ∼ 0.01 days^{−1}), the time lag increases with increasing Eddington ratio at low mass, and this positive correlation weakens or even becomes slightly negative as mass increases.

$\log(m) \equiv \log(M_{\text{BH}}/M_{\odot})$, and $\log(\dot{m})$. The best-fitting results are

$$\beta = -0.2792 \log(m) - 0.0248 \log(\dot{m}) + 0.0161 \log^2(m) + 0.0156 \log^2(\dot{m}) + 1.7438, \quad (10)$$

$$f_0 = -0.0441 \log(m) + 0.0014 \log(\dot{m}) + 0.0029 \log^2(m) + 0.0025 \log^2(\dot{m}) + 0.1637, \quad (11)$$

$$T_0 = 0.0038 \log(\dot{m}) + 0.0011 \log^2(\dot{m}) + 0.0186. \quad (12)$$

These can be used for predicting the CHAR model lags of sources with various M_{BH} and \dot{m} .

We also use the supervised machine learning algorithm, Random Forest (hereafter RF; Breiman 2001), to learn the relation $T_{\text{lag}} = g(f, \lambda, M_{\text{BH}}, \dot{m})$. In the Random Forest, a decision tree is a hierarchical structure that makes successive partitions of the data with a set of if-then-else decision rules. The random forest algorithm is an ensemble technique that combines multiple decision trees on various sub-samples of the data set and uses averaging to improve the predictive accuracy and control over-fitting.

We used the scikit-learn (Pedregosa et al. 2011) Python package implementation of RF², building multiple regression model on T_{lag} with $f, \lambda, M_{\text{BH}}$, and \dot{m} as independent variables in logarithmic space. Again, we only consider frequencies whose corresponding time lags correlate with λ (i.e., $r^2 > 0.9$). We then randomly split the simulated lags into training and testing sets of 70% and 30%, respectively. We present our best hyperparameters in Table 1 obtained by `sklearn.model_selection.GridSearchCV` (parameters that are not mentioned in the table are left as default values). We use the R^2 score and the mean squared error (MSE) to evaluate the predictions of the model. The R^2 and MSE of the training set and testing set are in Table 2. We also use NGC 5548 and Mrk 817 to test machine learning prediction. Overall, the machine learning result is good and accurate, and they can also be used to predict the frequency-resolved lags in various AGNs. The machine-learning model is slightly more accurate than the analytical results. Our machine-learning model is packaged as a PKL file and can be downloaded from <https://doi.org/10.12149/101308>.

² <https://scikit-learn.org/stable/modules/generated/sklearn.ensemble.RandomForestRegressor>

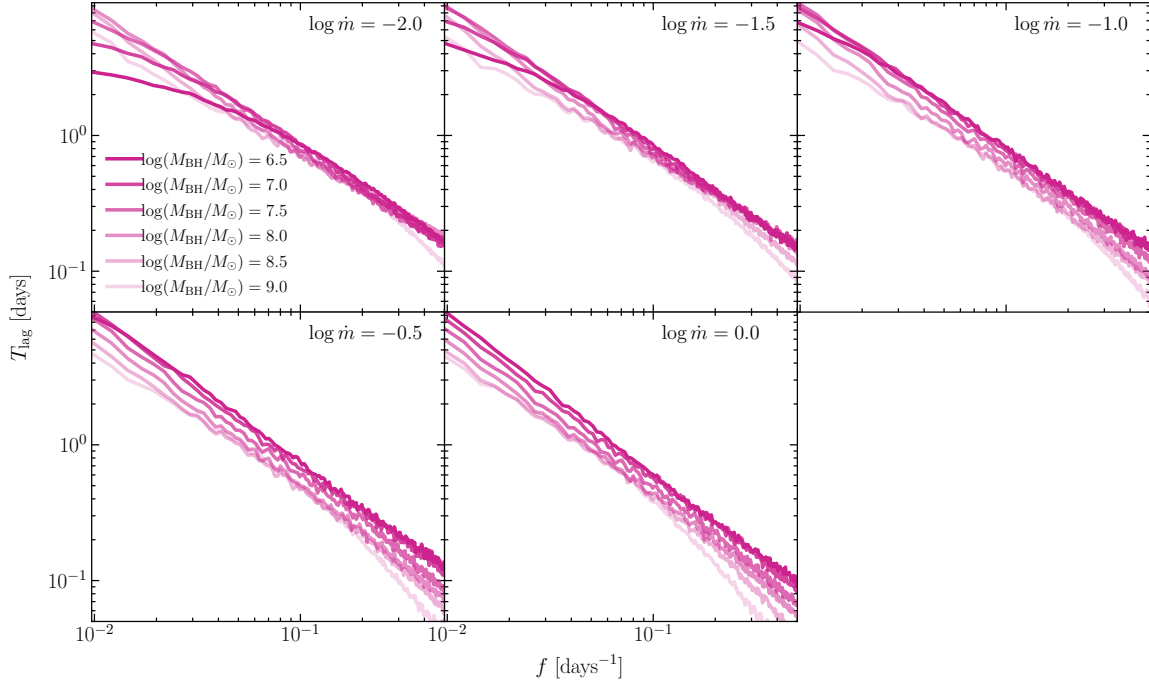


Figure 5. Simulated frequency-resolved lags of 5404 Å (i.e., V band) vs 1158 Å for the 30 cases. The frequency range is 0.097–0.5 days⁻¹. Each panel represents the frequency-lag relation at a fixed Eddington ratio for different black-hole masses. The lighter pink color corresponds to a larger black-hole mass. On the low-frequency region (e.g., ~ 0.01 days⁻¹), the time lag increases with increasing mass at low Eddington ratios, and this positive correlation weakens or even becomes slightly negative as the Eddington ratio increases.

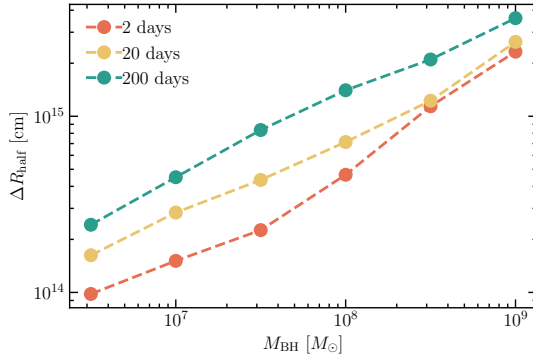


Figure 6. The difference between $R_{\text{half},5404}$ and $R_{\text{half},1158}$ in a range of black-hole masses with $\dot{m} = 0.1$. The timescale is the time duration of the variable flux. The longer timescale and larger black-hole mass result in larger ΔR_{half} .

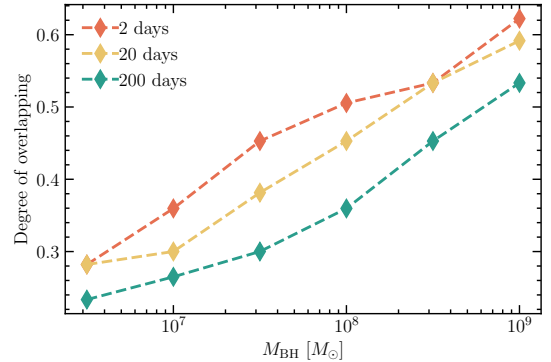


Figure 7. Degree of the emission-region overlapping between the 5404 Å (i.e., V band) and 1158 Å emission in a range of black-hole masses with $\dot{m} = 0.1$. The shorter timescale and larger black-hole mass result in more overlapping.

5. CONTINUUM LAG-LUMINOSITY RELATION

The continuum time lag-luminosity relation can probe the origin of AGN UV/optical variability. It is often argued that the observed continuum time lag-luminosity relation with a slope of 0.5 resembles the classical BLR radius-luminosity relation (Bentz et al. 2013). Hence, it is proposed that the observed continuum lags are echoes

of the diffuse continua from inner BLR clouds (e.g., Guo et al. 2022; Montano et al. 2022; Netzer 2022). In actual UV/optical observation, the luminous quasars are observed for longer time spans (i.e., the length of time for the monitoring campaign) than their faint counterparts because the formers are generally less variable than the latters (e.g., MacLeod et al. 2010; Sun et al. 2018b). For example, for the low-luminosity source, NGC 4593 ($L_{\text{bol}} = 7.8 \times 10^{43}$ erg s⁻¹), the time span of the time-lag

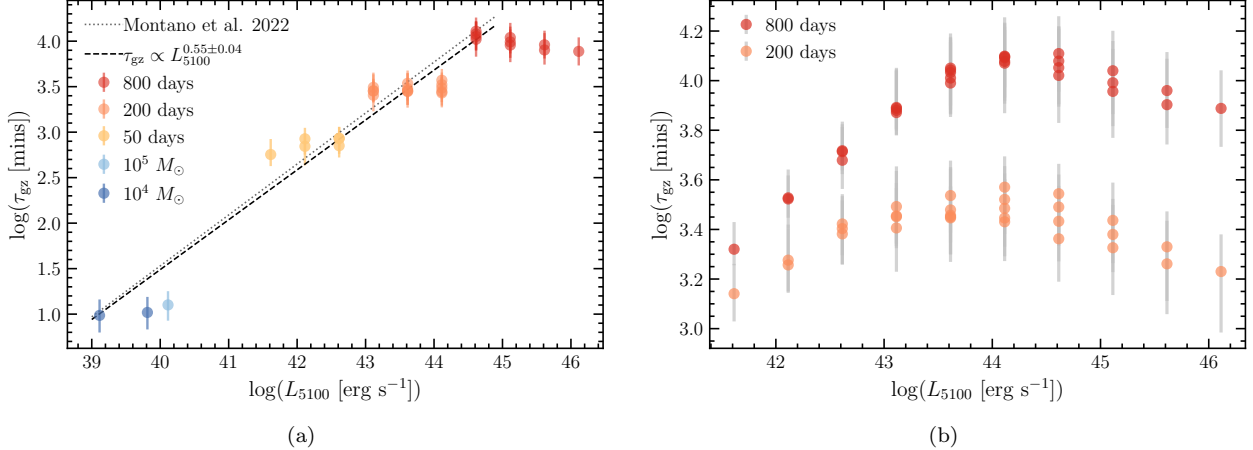


Figure 8. (a) τ_{gz} vs L_{5100} from the CHAR model for the 30 mock cases mentioned in Section 4 and 3 additional low-mass cases introduced in Section 5. Their M_{BH} and \dot{m} are mentioned in the first paragraph of Section 4 and the second paragraph of Section 5, respectively. The error bars are 25-th and 75-th percentiles. The black dashed line is the best-fitting to data points with $10^{39} < L_{5100} < 10^{45}$ erg s $^{-1}$. The grey dotted line is the observational fitting result from Montano et al. (2022). Note that several data points overlap at the same luminosity and have different M_{BH} and \dot{m} . (b) τ_{gz} vs L_{5100} for time spans of 200 days and 800 days for the 30 mock cases mentioned in Section 4. A longer time span results in a larger time lag; a decreasing trend appears at high luminosity in the same time span; the critical luminosity, below which this decreasing trend shows, is associated with the time span.

Table 1. Hyperparameters setting for RF

Model	Hyperparameters	Value
RF	n_estimators	80
	oob_score	<i>True</i>

NOTE—Other parameters not mentioned are left as default.

Table 2. Evaluation of RF

Set	R^2	MSE
Training set	0.9991	0.0003
Testing set	0.9938	0.0018
NGC 5548	0.998	0.001
Mrk 817	0.996	0.002

NOTE— R^2 and MSE are close to 1 and 0, respectively, indicating the RF model is accurate.

the time span is about 200 days (Edelson et al. 2015; Fausnaugh et al. 2016) in the rest-frame; for luminous quasars (e.g., Guo et al. 2022), the time span (in rest-frame) is about 800 days in the rest-frame. Inspired by the anti-correlation between the variability frequency and time lag, the differences in the time spans can induce the following observational bias: in order to measure inter-band time lags, the reverberation-mapping campaigns of luminous sources require longer time spans and thus have longer time lags than faint ones. We speculate that this bias may be responsible for the observed lag-luminosity relation. Hence, we are motivated to check the time lag-luminosity relation of the CHAR model.

We use the 30 mock cases, whose M_{BH} and \dot{m} are introduced in the first paragraph of Section 4, to calculate the time lag-luminosity relation of the CHAR model. We obtain the continuum luminosity $L_{5100} = \lambda L_{\lambda}$ at 5100 Å, which is empirically converted by $L_{\text{bol}} = 10L_{5100}$ (Hopkins et al. 2007). We split 30 mock sources into three luminosity bins and set the time span of 50 days in the low luminosity ($L_{5100} < 10^{43}$ erg s $^{-1}$), 200 days in the middle luminosity ($10^{43} < L_{5100} < 5 \times 10^{44}$ erg s $^{-1}$), and 800 days in the high luminosity ($L_{5100} > 5 \times 10^{44}$ erg s $^{-1}$). This setting is roughly consistent with the time spans of real continuum reverberation mapping programs in these luminosity ranges. The cadence of simulated light curves is 0.5 days. To extend the low-luminosity end to cover NGC 4395 ($L_{\text{bol}} = 5.3 \times 10^{40}$ erg s $^{-1}$; Moran et al. 2005), we consider low-mass mock AGNs of $M_{\text{BH}} = 10^4 M_{\odot}$, $\dot{m} = 0.01$ and

observations is 22.6 days (McHardy et al. 2018) in the rest-frame; for NGC 5548 ($L_{\text{bol}} = 3.2 \times 10^{44}$ erg s $^{-1}$),

0.05, and $M_{\text{BH}} = 10^5 M_{\odot}$, $\dot{m} = 0.01$. The time span for the three low-mass mock AGNs is one day (e.g., Montano et al. 2022) with a cadence of 0.005 days (i.e., seven minutes). Note that all mentioned timescales are in the rest frame. We use the CHAR model to generate multi-band light curves for these mock sources.

To compare the lag-luminosity relation of the CHAR model with observations (e.g., Guo et al. 2022; Montano et al. 2022; Netzer 2022), we use PYCCF (Sun et al. 2018a) to measure CHAR model mock light curves. Following Montano et al. (2022), we calculate the inter-band lag (τ) of the z band (9157 Å) with respect to the g band (4476 Å). We always perform a first-order polynomial detrending for all light curves prior to lag measurements to remove the long-term trend (Welsh 1999).

We obtain the median model lags and their 1σ uncertainties from the 128 CHAR simulations, as shown in Fig. 8(a). In the range of $10^{39} < L_{5100} < 10^{45}$ erg s $^{-1}$, we use the least square method to fit a linear relationship between time lags and luminosity in logarithmic space,

$$\log(\tau_{\text{gz}}/\text{mins}) = a \log(L_{5100}/\text{erg s}^{-1}) + b. \quad (13)$$

The best-fitting results and their 1σ uncertainties are $a = 0.55^{+0.04}_{-0.04}$, $b = -20.44^{+1.42}_{-1.42}$. The uncertainties of the slope and intercept are calculated following Hogg et al. (2010), assuming that the distributions of measured time lags are normal. The slope and intercept are almost identical to the observational results for local AGNs from Montano et al. (2022), who obtained $a = 0.56^{+0.05}_{-0.04}$, $b = -20.87^{+1.88}_{-1.96}$. Hence, the CHAR model can reproduce the lag-luminosity relation with a slope of ~ 0.5 without the diffuse continua from the BLR.

To discuss the relationship between the CCF lags and time span, we set the same time span of 30 mock sources mentioned in Section 4 to 200 days and 800 days, respectively. We calculate the corresponding time lag τ_{gz} . The median model lags and their 1σ uncertainties from the 128 CHAR simulations are presented in Fig. 8(b). It shows that the time span significantly impacts the lag-luminosity relation, i.e., a longer time span results in a larger time lag. This is because the signal with a longer time span contains more low-frequency components. Fig. 8(b) also shows that the lag-luminosity relation changes if the same time span is set. Overall, the tests in Fig. 8 indicate that the continuum lag-luminosity relation from observations may be partly caused by the differences in the time spans, i.e., the luminous sources are designed to have longer time-span observations than those of faint ones because quasar variability anti-correlates with luminosity (e.g., Kelly et al.

2009; MacLeod et al. 2010; Sun et al. 2018c; Suberlak et al. 2021).

Another striking feature in Fig. 8(b) is the decreasing trend in the time lags for high-luminosity mock sources ($L_{5100} > 10^{44}$ erg s $^{-1}$) under the same time span; this tendency deviates from the positive correlation for less luminous sources. The possible reasons for decreasing the time lags are the increasing overlap of the emission regions due to the larger M_{BH} , and the larger variability timescale in luminous sources (see Appendix A & B). The critical luminosity from the positive to the negative trend depends upon the time span. For example, it occurs near $L_{5100} \simeq 10^{44}$ erg s $^{-1}$ in 200 days, and near $L_{5100} \simeq 4 \times 10^{44}$ erg s $^{-1}$ in 800 days.

Within the existing AGN observations, there are limited time-lag measurements for high-luminosity sources with L_{5100} greater than 10^{45} erg s $^{-1}$. Hence, this decreasing trend has not yet been critically tested. For luminous AGNs, the time-lag measurement is more difficult than faint targets because the variations decrease with increasing luminosity (e.g., Kelly et al. 2009; MacLeod et al. 2010; Sun et al. 2018c; Suberlak et al. 2021). In addition, luminous AGNs are often at high redshift, and one should use infrared light curves to probe the rest-frame g and z bands. In general, the time-lag measurements of high-luminosity sources should be considered in future observations like LSST (Ivezić et al. 2019). Unlike the CHAR model, the BLR diffuse continuum model does not have such a critical luminosity. Hence, future LSST observations can be used to distinguish the two models.

6. SUMMARY

We have made the CHAR model predictions for the frequency-resolved lags in UV/optical reverberation mappings. Our main results can be summarized as follows.

1. We have used the simulated light curves of the CHAR model to reproduce the frequency-resolved lags of NGC 5548 and Mrk 335 quantitatively (see Figures 1 and 2; Section 3).
2. We have made predictions for the frequency-resolved lags in Mrk 817 (the target for the AGN STORM II program) and for other sources with a range of black-hole masses and Eddington ratios. We have obtained the time lags as a function of the variability frequency, wavelength, black-hole mass, and Eddington ratio (see Figures 3, 4 and 5; Sections 3 and 4).
3. The continuum lag-luminosity relation obtained from observations may be partly caused by the dif-

ferences in the time span, i.e., the reverberation-mapping campaigns of luminous sources are designed to have longer time spans than those of faint ones because quasar variability anti-correlates with luminosity. Hence, the continuum time lag-luminosity relation might have nothing to do with the BLR (see Figure 8; Section 5).

4. For the same time span, the time lags are positively correlated with luminosity and show a decreasing trend at high luminosity. The critical luminosity in the decreasing trend increases with the time span (see Figure 8(b); Section 5).

Therefore, the CHAR model can explain many observational facts about AGN UV/optical reverberation mappings, i.e., the frequency-resolved lags for NGC 5548 and Mrk 335. We find that the measured lags in UV/optical reverberation mappings are influenced by many factors, such as observation duration (frequency), variability timescale, and overlapping of emission regions. Therefore, it may be inaccurate to use time lags to simply represent the size of the accretion disk, especially for high-luminosity sources. The continuum lag-luminosity relation from current observations needs to be tested more rigorously. More future observations can help us critically test the CHAR model and understand AGN physics.

ACKNOWLEDGEMENTS

We thank Shuo Liu for the helpful discussion about machine learning. We thank the referee for his/her useful comments that improve the manuscript. C.J. and M.Y.S. acknowledge support from the National Natural Science Foundation of China (NSFC-11973002), the Natural Science Foundation of Fujian Province of China (No. 2022J06002), and the China Manned Space Project grant (No. CMS-CSST-2021-A06 and CMS-CSST-2021-B11). Z.X.Z. acknowledges support from the National Natural Science Foundation of China (NSFC-12033006 and NSFC-12103041). C.J. acknowledges the support from the Undergraduate Innovation Program of Xiamen University.

¹ *Software:* AstroML (VanderPlas et al. 2012),
² Jupyter notebooks (Perez & Granger 2007), Matplotlib
³ (Hunter 2007), Numpy & Scipy (van der Walt et al.
⁴ 2011), PYCCF (Sun et al. 2018a), SCIKIT-LEARN (Pe-
⁵ dregosa et al. 2011).

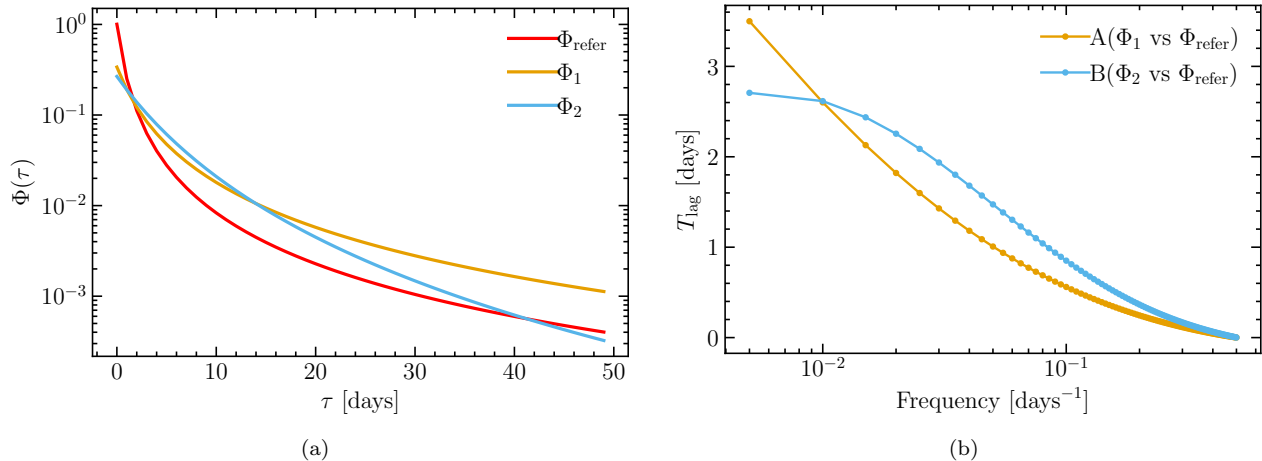


Figure 9. (a) Three types of response functions. Three response functions have centroids of 4.33, 9.83, and 5.58 days and medians of 0.99, 2.91, and 2.92 days, respectively. (b) The analytical frequency-resolved lags in two cases, A(Φ_1 vs Φ_{refer}) and B(Φ_2 vs Φ_{refer}). At frequencies higher than $1/(2\pi \times 14) \text{ days}^{-1}$, the time lags of case A are lower than case B because the response function Φ_1 is less extended than Φ_2 .

APPENDIX

A. THE OVERLAPPING EFFECT IN THE MEASURED LAGS

In a linearized RM model, the observed light curves are the convolution of the same underlying variable signal with the response function $\Phi(\tau)$ (Blandford & McKee 1982). Given the response functions of two light curves, we can calculate the frequency-resolved lags by eq. 10 from Cackett et al. (2022), i.e., the lags of the product of the Fourier transforms of two response functions. To show the diluted effect in the measured lags, we consider three types of normalized response functions shown in Fig. 9(a), $\Phi_{\text{refer}}(\tau) = 1.005/(\tau + 1)^2$, $\Phi_1(\tau) = 3.045/(\tau + 3)^2$, and $\Phi_2(\tau) = 4272.13/(\tau + 11.25)^4$, respectively. The range for τ is from 0 to 200 days, and the constants on the numerators are the corresponding normalized coefficients. Three response functions have centroids of 4.33, 9.83, and 5.58 days, and medians (i.e., the cumulative contribution fraction equals 0.5) of 0.99, 2.91, and 2.92 days, respectively. Φ_{refer} represents the response function of the short wavelength, while Φ_1 and Φ_2 are for long wavelength but have different distributions. Φ_1 have a larger centroid lag than Φ_2 . For $\tau < 14$ days, Φ_2 is more extended than Φ_1 , while for $\tau > 14$ days, Φ_1 is more extended than Φ_2 . We calculate the frequency-resolved lags between Φ_{refer} and Φ_1 (hereafter case A) or between Φ_{refer} and Φ_2 (hereafter case B), shown in Fig. 9(b). At frequencies greater than $1/(2\pi \times 14) \text{ days}^{-1}$, the lags in case A are systematically smaller than in case B. At frequencies smaller than $1/(2\pi \times 14) \text{ days}^{-1}$, the lags in case A are larger than in case B. Overall, if the emission regions of the short wavelength significantly overlap with those of the long wavelength, the frequency-resolved lags will be reduced over a wide frequency range.

B. THE VARIABILITY TIMESCALE AFFECTS THE MEASURED LAGS

The thermal timescale ($\tau_{\text{TH}} \sim 1/(\alpha\Omega_K)$) in the CHAR model represents the gas temperature fluctuation timescale, which increases with increasing radius and black-hole mass. Hence, different sources can have different characteristic variability timescales. We find that the variability timescale can also affect the frequency-resolved time lags. To illustrate this effect, we take the Damped Random Walk (hereafter DRW) model as an example. The light-curve generating algorithm is from AstroML Python package³. One parameter of the DRW model is the damping timescale τ_{DRW} . We generate 410-day-long DRW signals in the same random state with four damping timescales of 30 days, 60 days, 100 days, and 130 days, respectively. Here, the damping timescales of 30 and 60 days represent the variability timescales of two light curves produced by a mock source, while 100 days and 130 days are for the other more luminous

³ https://www.astroml.org/modules/generated/astroML.time_series.generate_damped_RW

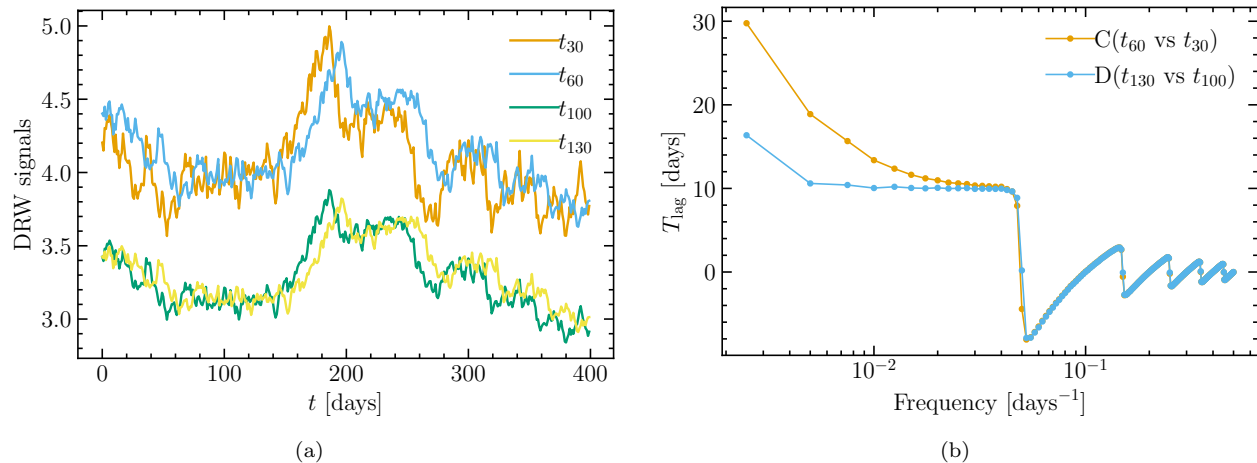


Figure 10. (a) The DRW light curves for the damping timescale $t_{\text{damp}} = 30$ days, 60 days, 100 days, and 130 days, respectively. All light curves are generated with the same random state; hence, these light curves are strongly correlated. The light curves with $t_{\text{damp}} = 30$ days or 100 days are shifted by 10 days (see text). (b) The 1000-times averaged frequency-resolved lags in two cases, $C(t_{60} \text{ vs } t_{30})$ and $D(t_{130} \text{ vs } t_{100})$.

mock source. The cadence of DRW signals is 1 day. These DRW signals are as a function of time (t ; in unit of days) denoted by y_{30} , y_{60} , y_{100} , and y_{130} , respectively. Then, we artificially shift the light curves $y_{30}(t)$ and $y_{100}(t)$ by 10 days and obtain two new light curves, i.e., $y'_{30}(t) = y_{30}(t + 10)$ and $y'_{100}(t) = y_{100}(t + 10)$. We calculate frequency-resolved lags between 400-day-long signals $y_{60}(t)$ and $y_{30}(t + 10)$ (hereafter case C) or between $y_{130}(t)$ and $y_{100}(t + 10)$ (hereafter case D). The simulation is repeated 1000 times, and the average lags as a function of f are shown in Fig. 10(b). It shows that at a fixed time span, the larger damping timescales result in smaller lags at the low-frequency regimes. Hence, this effect may also explain the reduced time lags in high luminosity sources.

C. THE FREQUENCY-RESOLVED LAGS UNCERTAINTY OF THE MODEL AND OBSERVATION

In the Fourier analysis, the uncertainties of the time lag at low and high frequencies are large. The former is due to the small number of low-frequency signals, while the latter is due to the significant influence of signal noise. Hence, the uncertainty of observation is related to the time duration and the signal-to-noise ratio. In our CHAR simulations for NGC 5548, Mrk 335, and Mrk 817, we use the same time duration as observations but do not consider the measurement errors of the light curves.

REFERENCES

- Bentz, M. C., Denney, K. D., Grier, C. J., et al. 2013, *ApJ*, 767, 149, doi: [10.1088/0004-637X/767/2/149](https://doi.org/10.1088/0004-637X/767/2/149)
- Blandford, R. D., & McKee, C. F. 1982, *ApJ*, 255, 419, doi: [10.1086/159843](https://doi.org/10.1086/159843)
- Breiman, L. 2001, *Machine Learning*, 45, 5, doi: [10.1023/A:1010933404324](https://doi.org/10.1023/A:1010933404324)
- Cackett, E. M., Bentz, M. C., & Kara, E. 2021, *iScience*, 24, 102557, doi: [10.1016/j.isci.2021.102557](https://doi.org/10.1016/j.isci.2021.102557)
- Cackett, E. M., Chiang, C.-Y., McHardy, I., et al. 2018, *ApJ*, 857, 53, doi: [10.3847/1538-4357/aab4f7](https://doi.org/10.3847/1538-4357/aab4f7)
- Cackett, E. M., Zoghbi, A., & Ulrich, O. 2022, *ApJ*, 925, 29, doi: [10.3847/1538-4357/ac3913](https://doi.org/10.3847/1538-4357/ac3913)
- Chelouche, D., Pozo Nuñez, F., & Kaspi, S. 2019, *Nature Astronomy*, 3, 251, doi: [10.1038/s41550-018-0659-x](https://doi.org/10.1038/s41550-018-0659-x)
- De Rosa, G., Peterson, B. M., Ely, J., et al. 2015, *ApJ*, 806, 128, doi: [10.1088/0004-637X/806/1/128](https://doi.org/10.1088/0004-637X/806/1/128)
- Donnan, F. R., Hernández Santisteban, J. V., Horne, K., et al. 2023, *MNRAS*, 523, 545, doi: [10.1093/mnras/stad1409](https://doi.org/10.1093/mnras/stad1409)
- Edelson, R., Gelbord, J. M., Horne, K., et al. 2015, *ApJ*, 806, 129, doi: [10.1088/0004-637X/806/1/129](https://doi.org/10.1088/0004-637X/806/1/129)
- Fausnaugh, M. M., Denney, K. D., Barth, A. J., et al. 2016, *ApJ*, 821, 56, doi: [10.3847/0004-637X/821/1/56](https://doi.org/10.3847/0004-637X/821/1/56)
- Fausnaugh, M. M., Starkey, D. A., Horne, K., et al. 2018, *ApJ*, 854, 107, doi: [10.3847/1538-4357/aaaa2b](https://doi.org/10.3847/1538-4357/aaaa2b)
- Gardner, E., & Done, C. 2017, *MNRAS*, 470, 3591, doi: [10.1093/mnras/stx946](https://doi.org/10.1093/mnras/stx946)
- Grier, C. J., Peterson, B. M., Pogge, R. W., et al. 2012, *ApJL*, 744, L4, doi: [10.1088/2041-8205/744/1/L4](https://doi.org/10.1088/2041-8205/744/1/L4)

- Guo, H., Barth, A. J., & Wang, S. 2022, *ApJ*, 940, 20, doi: [10.3847/1538-4357/ac96ec](https://doi.org/10.3847/1538-4357/ac96ec)
- Hogg, D. W., Bovy, J., & Lang, D. 2010, arXiv e-prints, arXiv:1008.4686, doi: [10.48550/arXiv.1008.4686](https://doi.org/10.48550/arXiv.1008.4686)
- Hopkins, P. F., Richards, G. T., & Hernquist, L. 2007, *ApJ*, 654, 731, doi: [10.1086/509629](https://doi.org/10.1086/509629)
- Huchra, J. P., Vogeley, M. S., & Geller, M. J. 1999, *VizieR Online Data Catalog*, *J/ApJS/121/287*, doi: [10.26093/cds/vizieR.21210287](https://doi.org/10.26093/cds/vizieR.21210287)
- Hunter, J. D. 2007, *Computing in Science and Engineering*, 9, 90, doi: [10.1109/MCSE.2007.55](https://doi.org/10.1109/MCSE.2007.55)
- Ivezić, Ž., Kahn, S. M., Tyson, J. A., et al. 2019, *ApJ*, 873, 111, doi: [10.3847/1538-4357/ab042c](https://doi.org/10.3847/1538-4357/ab042c)
- Kammoun, E. S., Papadakis, I. E., & Dovčiak, M. 2019, *ApJL*, 879, L24, doi: [10.3847/2041-8213/ab2a72](https://doi.org/10.3847/2041-8213/ab2a72)
- . 2021a, *MNRAS*, 503, 4163, doi: [10.1093/mnras/stab725](https://doi.org/10.1093/mnras/stab725)
- . 2021b, *MNRAS*, 503, 4163, doi: [10.1093/mnras/stab725](https://doi.org/10.1093/mnras/stab725)
- Kammoun, E. S., Robin, L., Papadakis, I. E., Dovčiak, M., & Panagiotou, C. 2023, *MNRAS*, 526, 138, doi: [10.1093/mnras/stad2701](https://doi.org/10.1093/mnras/stad2701)
- Kara, E., Mehdipour, M., Kriss, G. A., et al. 2021, *ApJ*, 922, 151, doi: [10.3847/1538-4357/ac2159](https://doi.org/10.3847/1538-4357/ac2159)
- Kara, E., Barth, A. J., Cackett, E. M., et al. 2023, *ApJ*, 947, 62, doi: [10.3847/1538-4357/acbcd3](https://doi.org/10.3847/1538-4357/acbcd3)
- Kelly, B. C., Bechtold, J., & Siemiginowska, A. 2009, *ApJ*, 698, 895, doi: [10.1088/0004-637X/698/1/895](https://doi.org/10.1088/0004-637X/698/1/895)
- King, A. R., Pringle, J. E., & Livio, M. 2007, *MNRAS*, 376, 1740, doi: [10.1111/j.1365-2966.2007.11556.x](https://doi.org/10.1111/j.1365-2966.2007.11556.x)
- Korista, K. T., & Goad, M. R. 2019, *MNRAS*, 489, 5284, doi: [10.1093/mnras/stz2330](https://doi.org/10.1093/mnras/stz2330)
- Lawther, D., Goad, M. R., Korista, K. T., Ulrich, O., & Vestergaard, M. 2018, *MNRAS*, 481, 533, doi: [10.1093/mnras/sty2242](https://doi.org/10.1093/mnras/sty2242)
- Lewin, C., Kara, E., Cackett, E. M., et al. 2023, arXiv e-prints, arXiv:2307.11145, doi: [10.48550/arXiv.2307.11145](https://doi.org/10.48550/arXiv.2307.11145)
- Li, T., Sun, M., Xu, X., et al. 2021, *ApJL*, 912, L29, doi: [10.3847/2041-8213/abf9aa](https://doi.org/10.3847/2041-8213/abf9aa)
- MacLeod, C. L., Ivezić, Ž., Kochanek, C. S., et al. 2010, *ApJ*, 721, 1014, doi: [10.1088/0004-637X/721/2/1014](https://doi.org/10.1088/0004-637X/721/2/1014)
- McHardy, I. M., Connolly, S. D., Horne, K., et al. 2018, *MNRAS*, 480, 2881, doi: [10.1093/mnras/sty1983](https://doi.org/10.1093/mnras/sty1983)
- Miller, L., Turner, T. J., Reeves, J. N., et al. 2010, *MNRAS*, 403, 196, doi: [10.1111/j.1365-2966.2009.16149.x](https://doi.org/10.1111/j.1365-2966.2009.16149.x)
- Montano, J. W., Guo, H., Barth, A. J., et al. 2022, *ApJL*, 934, L37, doi: [10.3847/2041-8213/ac7e54](https://doi.org/10.3847/2041-8213/ac7e54)
- Moran, E. C., Eracleous, M., Leighly, K. M., et al. 2005, *AJ*, 129, 2108, doi: [10.1086/429522](https://doi.org/10.1086/429522)
- Netzer, H. 2022, *MNRAS*, 509, 2637, doi: [10.1093/mnras/stab3133](https://doi.org/10.1093/mnras/stab3133)
- Pedregosa, F., Varoquaux, G., Gramfort, A., et al. 2011, *Journal of Machine Learning Research*, 12, 2825, doi: [10.48550/arXiv.1201.0490](https://doi.org/10.48550/arXiv.1201.0490)
- Perez, F., & Granger, B. E. 2007, *Computing in Science and Engineering*, 9, 21, doi: [10.1109/MCSE.2007.53](https://doi.org/10.1109/MCSE.2007.53)
- Peterson, B. M., Wanders, I., Horne, K., et al. 1998, *PASP*, 110, 660, doi: [10.1086/316177](https://doi.org/10.1086/316177)
- Roming, P. W. A., Kennedy, T. E., Mason, K. O., et al. 2005, *SSRv*, 120, 95, doi: [10.1007/s11214-005-5095-4](https://doi.org/10.1007/s11214-005-5095-4)
- Shakura, N. I., & Sunyaev, R. A. 1973, *A&A*, 24, 337
- Strauss, M. A., & Huchra, J. 1988, *AJ*, 95, 1602, doi: [10.1086/114757](https://doi.org/10.1086/114757)
- Suberlak, K. L., Ivezić, Ž., & MacLeod, C. 2021, *ApJ*, 907, 96, doi: [10.3847/1538-4357/abc698](https://doi.org/10.3847/1538-4357/abc698)
- Sun, M., Grier, C. J., & Peterson, B. M. 2018a, *PyCCF: Python Cross Correlation Function for reverberation mapping studies*, *Astrophysics Source Code Library*, record ascl:1805.032. <http://ascl.net/1805.032>
- Sun, M., Xue, Y., Cai, Z., & Guo, H. 2018b, *ApJ*, 857, 86, doi: [10.3847/1538-4357/aab786](https://doi.org/10.3847/1538-4357/aab786)
- Sun, M., Xue, Y., Trump, J. R., & Gu, W.-M. 2019, *MNRAS*, 482, 2788, doi: [10.1093/mnras/sty2885](https://doi.org/10.1093/mnras/sty2885)
- Sun, M., Xue, Y., Wang, J., Cai, Z., & Guo, H. 2018c, *ApJ*, 866, 74, doi: [10.3847/1538-4357/aae208](https://doi.org/10.3847/1538-4357/aae208)
- Sun, M., Xue, Y., Brandt, W. N., et al. 2020, *ApJ*, 891, 178, doi: [10.3847/1538-4357/ab789e](https://doi.org/10.3847/1538-4357/ab789e)
- Tie, S. S., & Kochanek, C. S. 2018, *MNRAS*, 473, 80, doi: [10.1093/mnras/stx2348](https://doi.org/10.1093/mnras/stx2348)
- Tripathi, S., McGrath, K. M., Gallo, L. C., et al. 2020, *MNRAS*, 499, 1266, doi: [10.1093/mnras/staa2817](https://doi.org/10.1093/mnras/staa2817)
- Uttley, P., Cackett, E. M., Fabian, A. C., Kara, E., & Wilkins, D. R. 2014, *A&A Rv*, 22, 72, doi: [10.1007/s00159-014-0072-0](https://doi.org/10.1007/s00159-014-0072-0)
- van der Walt, S., Colbert, S. C., & Varoquaux, G. 2011, *Computing in Science and Engineering*, 13, 22, doi: [10.1109/MCSE.2011.37](https://doi.org/10.1109/MCSE.2011.37)
- VanderPlas, J., Connolly, A. J., Ivezić, Z., & Gray, A. 2012, in *Proceedings of Conference on Intelligent Data Understanding (CIDU)*, 47–54, doi: [10.1109/CIDU.2012.6382200](https://doi.org/10.1109/CIDU.2012.6382200)
- Welsh, W. F. 1999, *PASP*, 111, 1347, doi: [10.1086/316457](https://doi.org/10.1086/316457)
- Yao, P. Z., Secunda, A., Jiang, Y.-F., Greene, J. E., & Villar, A. 2023, *ApJ*, 953, 43, doi: [10.3847/1538-4357/acde7e](https://doi.org/10.3847/1538-4357/acde7e)
- Zoghbi, A., Reynolds, C., & Cackett, E. M. 2013, *ApJ*, 777, 24, doi: [10.1088/0004-637X/777/1/24](https://doi.org/10.1088/0004-637X/777/1/24)